Acta Biomaterialia 151 (2022) 501–511

Contents lists available at ScienceDirect

Acta Biomaterialia

journal homepage: www.elsevier.com/locate/actbio

Full length article

# Injectable mesoporous bioactive nanoparticles regenerate bone tissue under osteoporosis conditions

D. Arcos[a,b,*], N. Gómez-Cerezo[a,b], M. Saiz-Pardo[c], D. de Pablo[c], L. Ortega[c], S. Enciso[d], B. Fernández-Tomé[d], I. Díaz-Güemes[d], F.M. Sánchez-Margallo[d], L. Casarrubios[e], M.J. Feito[e], M.T. Portolés[b,e,*], M. Vallet-Regí[a,b,*]

[a] Departamento de Química en Ciencias Farmacéuticas, Facultad de Farmacia, Universidad Complutense de Madrid, Instituto de Investigación Sanitaria Hospital 12 de Octubre i+12, Plaza Ramón y Cajal s/n, 28040 Madrid, Spain
[b] CIBER de Bioingeniería, Biomateriales y Nanomedicina, CIBER-BBN, 28040 Madrid, Spain
[c] Servicio de Anatomía Patológica, Hospital Clínico San Carlos, Facultad de Medicina Universidad Complutense de Madrid, Instituto de Investigación Sanitaria Hospital Clínico San Carlos (IdISSC), 28040 Madrid, Spain
[d] Centro de Cirugía de Mínima Invasión Jesus Usón, NANBIOSIS, Cáceres, Spain
[e] Departamento de Bioquímica y Biología Molecular, Facultad de Ciencias Químicas, Universidad Complutense de Madrid, Instituto de Investigación Sanitaria del Hospital Clínico San Carlos (IdISSC), 28040 Madrid, Spain

ARTICLE INFO

*Article history:*
Received 2 June 2022
Revised 7 July 2022
Accepted 29 July 2022
Available online 3 August 2022

*Keywords:*
Mesoporous bioactive nanoparticles
Osteoporosis
Bone regeneration
Ipriflavone
Hyaluronic acid

ABSTRACT

The osteogenic capability of mesoporous bioactive nanoparticles (MBNPs) in the $SiO_2$–CaO system has been assessed *in vivo* using an osteoporotic rabbit model. MBNPs have been prepared using a double template method, resulting in spherical nanoparticles with a porous core-shell structure that has a high surface area and the ability to incorporate the anti-osteoporotic drug ipriflavone. *In vitro* expression of the pro-inflammatory genes NF-$\kappa$B1, IL-6, TNF-$\alpha$, P38 and NOS2 in RAW-264.7 macrophages, indicates that these nanoparticles do not show adverse inflammatory effects. An injectable system has been prepared by suspending MBNPs in a hyaluronic acid-based hydrogel, which has been injected intraosseously into cavitary bone defects in osteoporotic rabbits. The histological analyses evidenced that MBNPs promote bone regeneration with a moderate inflammatory response. The incorporation of ipriflavone into these nanoparticles resulted in a higher presence of osteoblasts and enhanced angiogenesis at the defect site, but without showing significant differences in terms of new bone formation.

**Statement of significance**

Mesoporous bioactive glass nanoparticles have emerged as one of the most interesting materials in the field of bone regeneration therapies. For the first time, injectable mesoporous bioactive nanoparticles have been tested *in vivo* using an osteoporotic animal model. Our findings evidence that MBG nanoparticles can be loaded with an antiosteoporotic drug, ipriflavone, and incorporated in hyaluronic acid to make up an injectable hydrogel. The incorporation of MBG nanoparticles promotes bone regeneration even under osteoporotic conditions, whereas the presence of IP enhances angiogenesis as well as the presence of osteoblast cells lining in the newly formed bone. The injectable device presented in this work opens new possibilities for the intraosseous treatment of osteoporotic bone using minimally invasive surgery.



## 1. Introduction

In the last decade, there has been growing interest in the incorporation of nanotechnology as a strategy for the treatment of osteoporosis and bone regeneration therapies [1–4]. The prevalence of osteoporosis is steadily increasing as the world's population has

* Corresponding authors.
*E-mail addresses:* arcosd@ucm.es (D. Arcos), portoles@quim.ucm.es (M.T. Portolés), vallet@ucm.es (M. Vallet-Regí).

https://doi.org/10.1016/j.actbio.2022.07.067

aged throughout the 20th and 21st centuries [5] and prevention of osteoporosis-related fractures remains an unmet clinical need [6].

One of the most interesting strategies for the treatment of osteoporosis is the development of formulations based on mesoporous bioactive glass (MBG) nanoparticles [7]. MBG nanoparticles are usually prepared in the $SiO_2$–CaO and $SiO_2$–CaO-$P_2O_5$ systems and present a set of very interesting characteristics for the treatment of osteoporotic bone. Although only a finite range of compositions are bioactive in these systems when are prepared by the sol-gel method, the incorporation of a structure directing agent, which significantly increases the surface area and porosity, facilitates the ionic exchange and provides more sites for the nucleation and crystallization of carbonate hydroxyapatite, very similar to mineral component of the bone when these materials are soaked in simulated body fluids [8]. These bioceramics are also potential candidates for dental applications such as treatment of dental hypersensitivity and dental pulp demineralization [9–11].

The mesoporous structure of MBG nanoparticles facilitates ion exchange with the surrounding fluids. This fact has attracted the attention of many researchers to the possibility of incorporating therapeutic ions within their inorganic phase. In this sense, different cations have been incorporated into $SiO_2$–CaO or $SiO_2$–CaO-$P_2O_5$ systems to provide osteogenic [12–14], antitumor [15,16], antibacterial [17–20] or the combination of several properties [21,22] to MBG nanoparticles. Moreover, the interest in MBG nanoparticles has promoted the development of different synthesis methods, such as ultrasound-assisted sol-gel [23,24], centrifugation-assisted sol-gel [25], microemulsions [26,27], spray pyrolysis [28] or double-template systems [29]. Regardless of the synthesis method used, all of them require the incorporation of at least one structure-directing agent, which forms an organized micellar system through a self-assembly process in combination with the precursors of the inorganic phase. Depending on the structure directing agent and the synthesis method, the morphology of the MBG nanoparticles can be designed as hollow mesoporous spheres [30–32], radial mesoporous particles [33,34], etc., which allows tailoring their characteristics as nanocarriers for drug loading and release.

In 2018, Pontremoli *et al.* reported the use of MBG nanoparticles as injectable platforms combined with hydrogels [35]. This strategy would open the possibility of delivering MBG nanoparticles as intraosseous biomaterials via minimally invasive surgery. Despite this promising strategy, *in vivo* studies on MBG nanoparticles are scarce [36–40] and, to our knowledge, no study has tested the bone regenerative capability of MBG nanoparticles in osteoporotic animal models.

In previous works, our research group has widely studied the *in vitro* response of different cell types to MBG nanoparticles. Those studies demonstrated that the intracellular incorporation of these nanoparticles loaded with ipriflavone (IP) decreased the proliferation and resorption activity of osteoclasts [41] and stimulated the differentiation of osteoprogenitor [9] and endothelial progenitor cells [42]. In this work, we have prepared MBG nanoparticles with and without ipriflavone (IP), in a similar way as we did previously. Several studies have suggested the clinical interest of IP for the treatment of postmenopausal osteoporosis due to its tolerability [43,44]. However, IP is not currently a drug of choice for the treatment of osteoporosis because of its poor pharmacological activity when administered orally. Some studies suggest that it might be mainly due to the intestinal first-pass effect [45]. Therefore, we hypothesize that local *in situ* administration of IP loaded on MBG nanoparticles could enhance bone regeneration under osteoporosis conditions. With this aim, we have carried out *in vivo* studies by implanting MBG nanoparticles with and without IP in the bone of osteoporotic rabbits. In order to prepare injectable materials, MBG nanoparticles were incorporated into a hyaluronic acid hydrogel. This step was performed in the operating room in the moments prior to implantation of the material. Hyaluronic acid was chosen on the basis of previous studies supporting its use as a carrier of cells and growth factors [46], as well as for its potential to enhance osteogenesis and mineralization [47]. On the other hand, prior to the *in vivo* studies, we evaluated and quantified by qPCR the expression of several pro-inflammatory genes in macrophages treated *in vitro* with these nanoparticles, in order to complete the immune response studies previously performed.

## 2. Materials and methods

### 2.1. Synthesis of mesoporous bioactive nanoparticles (MBNPs)

MBNPs of nominal composition 75 $SiO_2$–20 CaO-5 $P_2O_5$ (% mol) were prepared by hydrolysis and condensation of tetraethylortosilicate (TEOS), triethylphosphate (TEP) and calcium nitrate tetrahydrate ($Ca(NO_3)_2{\cdot}4H_2O$), in the presence of poly(styrene)-block-poly(acrylic acid) (PS-b-PAA) and hexadecyltrimethylammonium bromide (CTAB), two different amphiphilic molecules that behave as structure directing agents as proposed by Li *et al.* [29]. 80 mg of PS-b-PAA were dissolved in 16 mL of tetrahydrofurane, subsequently poured onto a solution of 160 mg of CTAB in 74 mL of D.I. water and 2.4 mL of ammonia (28% w/w). The mixture was magnetically stirred vigorously for 20 min at room temperature to form an o/w nanoemulsion. Thereafter, 25 $\mu$L of TEP in 1.6 mL of ethanol, 0.52 mL of TEOS in 1.6 mL of ethanol and 125 mg of $Ca(NO_3)_2{\cdot}4H_2O$ in 1.6 mL of water were added dropwise in 20 minutes' intervals. The recipient was covered by two layers of parafilm to avoid the evaporation of volatile compounds and the mixture was magnetically stirred for additional 24 h. After this period, the nanoparticles were collected by centrifugation at 10,000 r.pm. ($g = 16.466$) for 10 min and thoroughly washed with a mixture of ethanol-water (50:50). The solid was dried at 30 °C under vacuum conditions and subsequently calcined from room temperature to 550 °C for 4 h using a heating rate of 1 °C $min^{-1}$ under air atmosphere. All reactants were purchased from Sigma- Aldrich (St. Louis, MO, USA).

### 2.2. Loading of ipriflavone (IP) in MBNPs

Ipriflavone (IP, 7-isopropoxy-3-phenyl-4H-1-benzopyran-4-one) was loaded in MBNPs by impregnation in a highly concentrated drug solution. For this aim, 400 mg of IP were dissolved in 6 mL of acetone. The solution was then filtered to remove the excess of drug without dissolving and 80 mg of nanoparticles were soaked in this solution and kept under orbital stirring for 24 h. IP loaded nanoparticles (MBNP-IP) were filtered under vacuum using a polyamide filter and thoroughly washed with a mixture of ethanol:water (50:50) to remove the excess of IP physically adsorbed on the outer surface of the nanoparticles.

### 2.3. Characterization techniques

MBNP and MBNP-IP were analysed by scanning electron microscopy (SEM) using a JEOL F-6335 microscope (JEOL Ltd., Tokyo, Japan), operating at 20 kV and equipped with an energy dispersive X-ray spectrometer (EDX). Previously, the samples were mounted on stubs and gold coated in vacuum using a sputter coater (Balzers SCD 004, Wiesbaden- Nordenstadt, Germany).

In order to study the mesoporous structure of the material, the nanoparticles were analysed by transmission electron microscopy (TEM) using a JEOL-1400 microscope (JEOL Ltd., Tokyo, Japan), operating at 300 kV (Cs 0.6 mm, resolution 1.7 Å). Images were recorded using a CCD camera (model Keen view, SIS analyses size

1024 × 1024, pixel size 23.5 mm x 23.5 mm) at 60000X magnification using a low-dose condition. Textural properties were determined by nitrogen adsorption analysis with a 3Flex analyser (Micromeritics, Norcross, GA, USA). The adsorption/desorption isotherms were obtained after degassing the samples at 150 °C for 15 h under vacuum.

The incorporation of IP was determined by Fourier Transform Infrared (FTIR) spectroscopy with a Nicolet Magma IR 550 spectrometer (Thermo Fisher Scientific, Waltham, Massachusetts, USA) and using the attenuated total reflectance (ATR) sampling technique with a Golden Gate accessory. Besides, thermogravimetrical analysis (TG) was carried out by triplicate with a Pyris Diamond TG/DTA analyser (PerkinElmer Instruments) to quantify the amount of IP loaded.

### 2.4. Expression of pro-inflammatory genes quantified by real-time PCR (qPCR)

RAW-264.7 cells (American Type Culture Collection, ATCC) were seeded in 6 well culture plates (Corning, USA), at a density of $10^6$ cells/mL, in 2 mL of Dulbecco's Modified Eagle Medium (DMEM) supplemented with 10% fetal bovine serum (FBS, Gibco, BRL), 1 mM L-glutamine (BioWhittaker Europe, Belgium), penicillin (200 $\mu$g/mL, BioWhittaker Europe, Belgium), and streptomycin (200 $\mu$g/mL, BioWhittaker Europe, Belgium) at 37 °C under a $CO_2$ (5%) atmosphere. After 24 h of culture in the presence or the absence of 50 $\mu$g/mL of MBNP or MBNP-IP, the attached RAW-264.7 cells were washed with phosphate buffered saline (PBS), harvested using cell scrapers and centrifuged at 310 g for 10 min. The pellets were treated as indicated below for analysis of the expression of the pro-inflammatory genes NF-$\kappa$B1, IL-6, TNF-$\alpha$, P38 and NOS2. Data were normalized to the expression levels of glyceraldehyde-3-phosphate dehydrogenase (GAPDH) as housekeeping gene. Specific primers were designed for qPCR, to be used in combination with "Universal Probe Library" probes (Roche Diagnostics). The design was done with the software "ProbeFinder Assay Design Software" (Roche Life Science) at https://lifescience.roche.com/en_es/brands/universal-probe-library.html#assay-design-center from *Mus musculus* gene sequences.

Oligonucleotides were synthesized by Metabion International AG. The primers and UPL (Universal Probe Library) probes used in the assay are shown in the Table 1. cDNA synthesis was carried out with the "High Capacity RNA to CDNA" kit (Applied Biosystems) and 1 µg of total RNA in 20 µL following the manufacturer's instructions (1 h 25 °C; 5 min 95 °C). For real-time quantitative PCR assays, the "TaqMan Gene Expression Master Mix" kit (Applied Biosystems) was used according to the manufacturer's instructions, with 2.5 µL of sample in 10 µL per assay, in 384-well PCR plates, and assayed in duplicate. Assays were performed on a "QuantStudio™ 12 K Flex" equipment (Applied Biosystems), with standard thermal conditions: 95 °C 10 min; 40 x (95 °C 15 s, 60 °C 1 min). Standard curves were prepared with serial dilutions of one of the samples to verify primer performance. Assays for the analysis of all samples were performed with 1/10 dilutions of cDNA. Data analysis and relative quantification, based on the DDCt algorithm, was carried out with "QuantStudio™ 12 K Flex Software".

**Table 1**
Primers used for RT-PCR analysis.

| Gene | Primers | UPL probes |
|---|---|---|
| NF-$\kappa$B1 | Nfkb1–69-F: CAGGTCCACTGTCTGCCTCT<br>Nfkb1–69-R: CCCGGAGTTCATCTATGTGC | 69 |
| IL-6 | IL6–78-F: TCCTACCCCAATTTCCAATG<br>IL6–78-R: GAATTGGATGGTCTTGGTCCT | 78 |
| TNF-$\alpha$ | TNFa-23-F: TGAAGGGAATGGGTGTTCAT<br>TNFa-23-R: GGGTCAGAGTAAAGGGGTCAG | 23 |
| P38 | P38–45-F: ACAGGCTACGTGGCTACCAG<br>P38–45-R: CGGTTATAGTGCATCCAATTCA | 45 |
| NOS2 | Nos2–2-F: GCTCATGACATCGACCAGAA<br>Nos2–2-R: TCCTCCTGCCCACTGAGTT | 2 |
| GAPDH | GAPDH-80-F: GTTCCTACCCCCAATGTATCC<br>GAPDH-80-R: CTGCTTCACCACCTTCTTGA | 80 |

### 2.5. In vivo studies

This study was approved by our Institutional Ethical Committee and by the regional Government of Extremadura (Spain), following the guidelines of the current normative (Directive 2010/63/EU of the European Parliament and of the Council of September 22, 2010, on the protection of animals used for scientific purposes).

#### 2.5.1. Osteoporosis model induction

Twelve adult female New Zealand rabbits (5.75 ± 0.35 kg) were used in this study. An acclimatization period of at least ten days was allowed before the start of the experimental procedure. The animals were housed individually (dedicated racks) at JUMISC's animal facilities under environmentally controlled conditions (12 h light/ 12 h dark; 16–22 °C; 30–70% RH). The feeding and care of the animals was carried out under current legislation on animal welfare. Animals were fed a standard maintenance diet for rabbit. Drinking water consisted of tap water administered by an automatic drink system (*ad libitum*). A laparoscopic bilateral ovariectomy was performed in all animals under aseptic conditions and general anesthesia. Animals were induced with propofol (4 mg/kg) and maintained on isoflurane in oxygen. Rabbits were administered intraoperatively meloxicam (0.6 mg/kg), buprenorphine (0.001 mg/kg) and enrofloxacine (10 mg/kg). The laparoscopic ovariectomy was performed using a median three portal technique (one 3.5 mm and two 5 mm trocars). The ovaries were removed after sealing the ovarian pedicle with LigaSure™ (Medtronic) and exteriorized by removing the 5 mm trocar. Postoperative analgesia was provided with meloxicam (0.6 mg/kg/24 h/3 days). Two weeks after, methylprednisolone sodium succinate (1 mg/kg/24 h/IM) was administered during 4 weeks, following the same protocol described elsewhere [48] in order to reproduce similar conditions as osteoporosis in humans.

#### 2.5.2. Implantation surgical procedure

Six weeks after the ovariectomy and immediately after methylprednisolone administration suppression, the biomaterials were blindly implanted in twelve rabbits (5.23 ± 0.68 kg) under aseptic conditions and the same anesthetic protocol described for laparoscopic ovariectomy. Two cylindrical defects (4 × 6 mm) were created in each rabbit by drilling the cancellous bone of the distal epiphysis of both femurs, under continuous irrigation with cold sterile saline.

MBNPs and MBNPS-IP were implanted as injectable materials by preparing a suspension of the nanoparticles in a hyaluronic acid-based hydrogel (HyStem™, Merck) in the operating room. For this aim, 1 mL of D.I water was added to one vial of thiol modified hyaluronic acid (Glycosyl®) and stirred in an incubator for 15 min. Once the solid was dissolved, 0.5 mL of this solution were added into a previously sterilized vial containing 20 mg of MBNPs or 23.6 mg of MBNPs-IP nanoparticles (20 mg of nanoparticles plus 3.6 mg of IP as calculated by TG, see below). The mixture was sonicated for 1 min, thus obtaining a homogeneous whitely suspension. Besides, 0.6 mL of D.I water was added to the thiol reactive crosslinker vial (Extralink®) and shaken until complete dissolution. Subsequently, 0.15 mL of crosslinker were poured onto the Glycosyl®- nanoparticles suspension. The mixture was loaded in a

1 mL syringe and after 2 min the gel acquired the appropriated viscosity to fill the defects. A small fraction of 40 mg of the as prepared injectable materials was used for the study by TG analysis and FTIR spectroscopy.

Once the biomaterials were randomly implanted, the deep and superficial subcutaneous layers were approximated with monofilament absorbable suture and the skin with braided absorbable suture following an intradermal closure. Six defects were left empty in order to prove that this bone defect model was critical enough and that any possible bone regeneration would be due to the injected material. Rabbits were administered enrofloxacine (10 mg/kg/24 h/5 days), buprenorphine (0.001 mg/kg/12 h/3 days), meloxicam (0.6 mg/kg/24 h/7 days) and metoclopramide (0.5 mg/kg/12 h/3 days). An accredited veterinarian checked the health condition of all animals daily along the whole study. Immediately after the surgical procedure and before the sample removal, a computed tomography (CT) scan was performed using a Philips Brilliance 6-slice CT scanner (Philips Healthcare CT software V2.3.0.1330). One of the rabbits that received a control defect and HA sample died during the anesthetic recovery after implantation surgery. At necropsy, hepatic degeneration and associated inflammatory symptoms were diagnosed as a secondary process. Therefore, biomaterials implanted were hyaluronic acid with MBNps ($n = 6$), hyaluronic acid with MBNPs-IP ($n = 6$) and hyaluronic acid as control material ($n = 5$), in addition to control defects ($n = 5$). After 12 weeks, the animals were euthanized under general anesthesia and samples were obtained.

### 2.5.3. Histological processing

At 12 weeks after implantation, the bone segments containing the defects were dissected out and fixed by immersion in 96% ethanol. Bone segments were processed as described elsewhere [49] and histological sections were stained with Haematoxylin-Eosin (Agilent Dako Coverstainer for H&E). The studies of angiogenesis and presence of inflammatory component were carried out by immunohystochemical analysis. For this purpose, FLEX Monoclonal Mouse Anti-Human CD34 Class II Clon QBEnd 10 Ready-to-Use (Dako Omnis) and FLEX Monoclonal Mouse Anti-Human CD45, Leucocyte Common Antigen Clones 2B11 + PD7/26 Ready-to-Use (Dako Omnis) were used. Bone tissue was fixed with formaldehyde and included in paraffin wax for immunohistochemistry (FLEX IHC Microscope Slides). Histological slides of 4 $\mu$m in thickness were obtained and pretreated with epitope recovery induced by heat (HIER), using an EnVision$^{TM}$ FLEX Target Retrieval Solution, High pH (50x) (Dako Omnis). Subsequently, paraffin was removed and the tissue was rehydrated and recovered using the Dako Omnis instrument. A combination of EnVision FLEX, High pH (Dako Omnis) and EnVision FLEX+ Mouse LINKER (Dako Omnis) was used as visualization system in the Dako Omnis instrument using hematoxylin as counterstain. Images were obtained by means of a Leica DMD1008 and an Olympus BX40 microscopes and analysed with ImageJ 1.x to calculate bone ingrowth area, trabeculae thickness and number of blood vessels. For the evaluation of angiogenesis, presence of inflammatory component and presence of osteoclasts, we used a four graded scale based on the density and distribution (absent/mild/moderate/marked, scored 0 to 3). Multinucleated cells located in a resorption lacuna were identified as osteoclasts. Oval cells with abundant blue-gray cytoplasm and perinuclear hofs, bordering the forming bone were identified as osteoblasts. (see Table S1 in supporting information)

### 2.5.4. Statistics

Results were expressed as mean ± standard error of mean (SEM). Statistical evaluation was carried out with the T-student test. All statistical tests were conducted at the two-sided 0.05 (p value) level of significance.

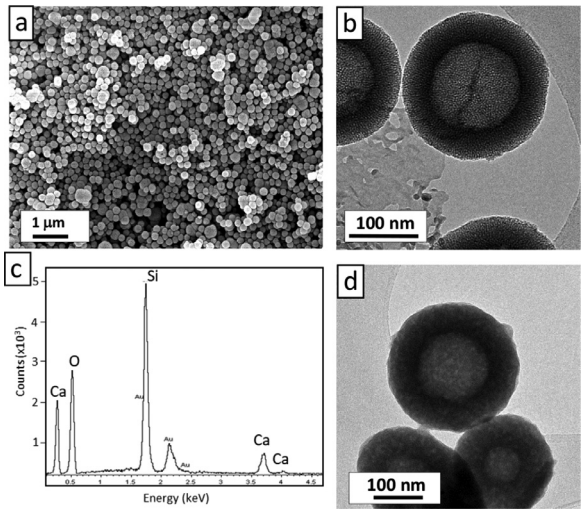


**Fig. 1.** Scanning electron micrograph of MBG nanoparticles (a); transmission electron image of MBG nanoparticles (b); EDX spectrum collected during TEM observation of MBG nanoparticles (c); transmission electron image of MBG nanoparticles after being loaded with ipriflavone.

## 3. Results

### 3.1. Characterization of mesoporous bioactive nanoparticles

Scanning electron micrograph obtained for MBNP sample (Fig. 1.a) shows spherical nanoparticles with homogeneous size distribution between 200 and 300 nm, although a few aggregates with sizes about 500 nm can be also observed. High-resolution electron transmission microscopy (HR-TEM) (Fig. 1.b) shows these MBNPs containing a dual mesoporous structure, consisting of an inner spherical mesoporous core surrounded by a shell exhibiting ordered mesopores with a radial distribution. EDX spectra collected during TEM observation (Fig. 1.c) showed a chemical composition of $SiO_2$ 81.54-CaO 18.56 (± 7.08) (% mol), calculated from 20 independent observations. No presence of phosphorous could be detected in any of the numerous observations accomplished. Finally, the TEM image of MBNP-IP (Fig. 1.d) evidences that the mesoporous structure is significantly deteriorated after drug loading, although the core-shell structure is still observed.

The textural properties of MBNP and MBNP-IP were determined by nitrogen adsorption analysis. The adsorption/desorption isotherms of MBNP (Fig. 2.a) show an adsorption branch characteristic of a mesoporus material. However, an irregular hysteresis loop is observed which can be explained in terms of a coexistence of two different mesoporous systems (core and shell). The bimodal pore size distribution obtained from desorption branch (inset in Fig. 2.a) shows two maxima centered at 2.6 and 4.3 nm, which is in agreement with the two mesoporous structures observed by TEM. These pores can be defined as mesopores according to the IUPAC nomenclature, which defines mesopores as pores with diameters between 2 and 50 nm. Besides, MBNPs exhibit high surface area and porosity (Table 2), as correspond to highly ordered mesoporous materials. After IP incorporation, the MBNP-IP isotherm (Fig. 2.d) shows the profile of a non-porous material, evidencing a very important loss of surface area and porosity (see Table 2) due to the filling of the pores by the drug

The presence and quantification of IP in MBNP-IP was confirmed by FTIR spectroscopy and TG analysis (Figure S2). After loading with IP, additional bands corresponding to the functional groups of the drug are observed in the FTIR spectra. TG analysis indicated a IP loading of 18 ± 1.2 (wt.%) within the MBNP-IP

**Table 2**
Textural parameters of MBG nanoparticles before and after being loaded with ipriflavone.

| | Surface area ($m^2g^{-1}$) | Pore volume ($cm^3g^{-1}$) | Pore size (nm) |
|---|---|---|---|
| MBNP | 543.63 (±1.02) | 0.435 (±0.017) | 2.62 / 4.33 (±0.02) |
| MBNP-IP | 14.42 (±0.09) | 0.059 (±0.005) | 10.57 (±0.07) |

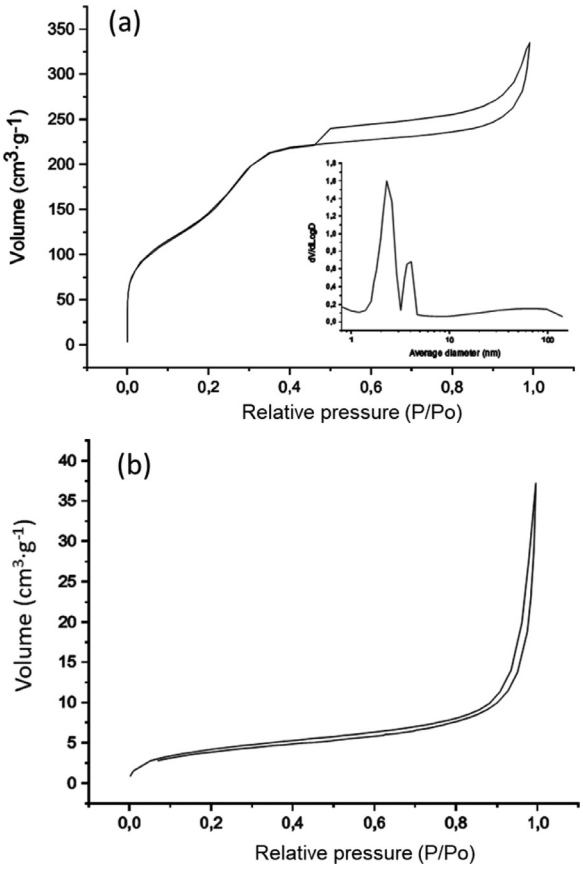


**Fig. 2.** Nitrogen adsorption/desorption isotherms for MBNP (a) and MBNP-IP (b). The inset shows the pore size distribution calculated from the desorption isotherm.

nanoparticles. (see section S2 in supporting information form more details).

TG analysis carried out the final injectable materials (see Figure S3 in supporting information), evidenced that the final mixture is mostly composed by water (around 95%) in both cases as expected for a hydrogel. The content in MBNP was considered to be the residual inorganic material after treating the sample at 600 °C under air atmosphere, showing values of 3.1 and 3.3 (% in mass) for MBNP and MBNP-IP, respectively. Finally, the amount of decomposed organic phase occurred between 110 °C and 600 °C was assigned to HA and HA plus ipriflavone for MBNP and MBNP-IP injectable materials, obtaining mass losses of 1.15 and 1.42 (% in mass), respectively. Besides, the FTIR spectra collected for injectable materials showed the absorption bands at 3000–3500 $cm^{-1}$ (O–H stretching vibration of $H_2O$ and HA), 1630 $cm^{-1}$ (bending scissor mode of $H_2O$) 2900 $cm^{-1}$ (weak shoulder, C–H stretching vibration of HA) 1408 $cm^{-1}$ (C–O stretching vibration of HA) and 1090 and 490 $cm^{-1}$ that correspond to Si-O stretching and Si-O-Si bending modes, respectively of MBNPs. Absorption bands for IP were masked mainly by the signals of $H_2O$ and HA and only a very weak signal at 1350 $cm^{-1}$ could be assigned to the presence of this drug.

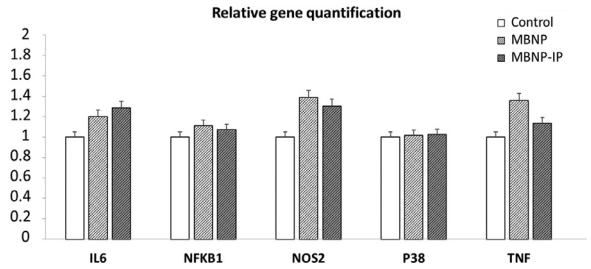


**Fig. 3.** Effects of 50 $\mu$g/mL of MBNP or MBNP-IP on the expression of the pro-inflammatory genes IL-6, NF-$\kappa$B1, NOS2, P38 and TNF-$\alpha$. Quantitative gene expression data were normalized to the expression levels of GAPDH as housekeeping gene. No significant differences were obtained in none of the cases with respect to the control.

### 3.2. Expression of pro-inflammatory genes quantified by qPCR

Expression of the pro-inflammatory genes NF-$\kappa$B1, IL-6, TNF-$\alpha$, P38 and NOS2 was quantified by qPCR (Fig. 3). *In vitro* studies did

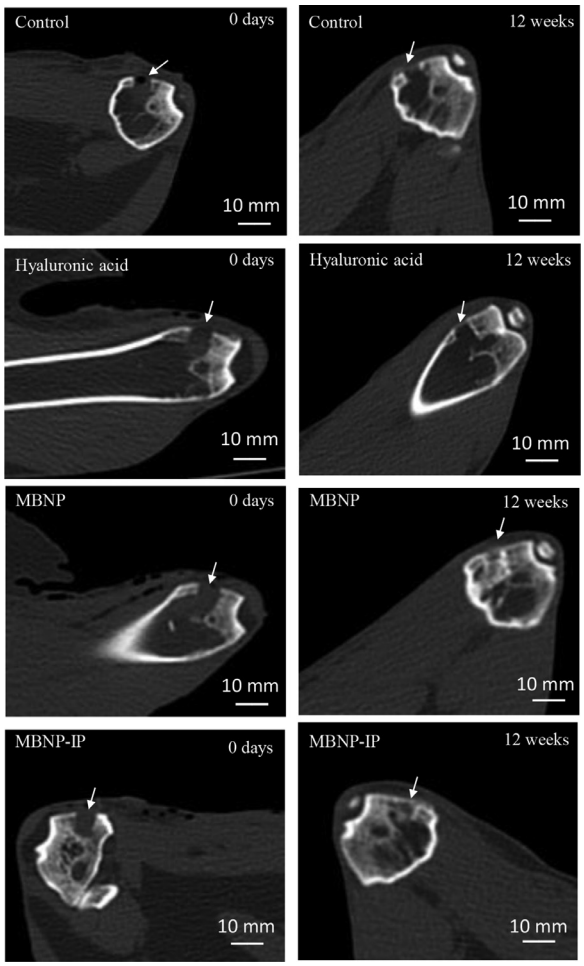


**Fig. 4.** CT scan images obtained just after implantation (0 days) and after 12 weeks of study.

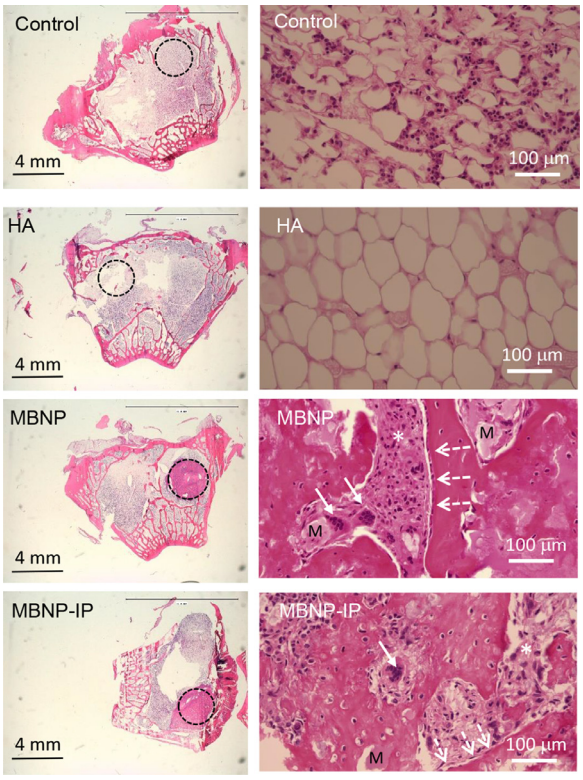


**Fig. 5.** Histological images after 12 weeks of implantation of control, hyaluronic acid, MBNP and MBNP-IP (left column: magnification x 3; right column: magnification x 20). Defect area is highlighted in low magnification images. Osteoblast lining (dotted arrows), osteoclasts (solid arrows) and inflammatory component (*) are pointed in high magnification images.

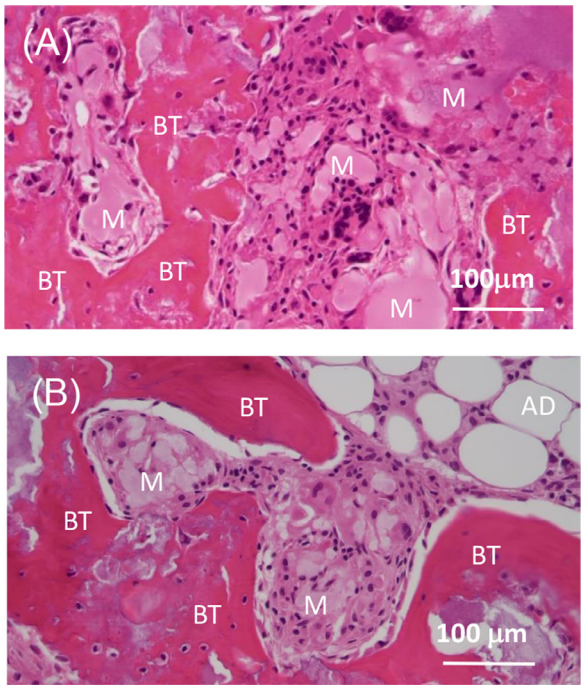


**Fig. 6.** Representative histological images after 12 week of implantation for (A) MBNP and (B) MBNP-IP. New formed bone tissue (BT) grows around injectable materials (M). Bone marrow mainly formed by adipocytes (AD) are also observed.

not show adverse inflammatory effects of these nanoparticles in terms of gene expression.

### 3.3. In vivo *studies*

#### 3.3.1. *Computer tomography (CT) scanning*

Fig. 4 shows the CT scan image collected just after post-operatory (0 days) and 12 weeks after implantation. The images in the left column were taken before the rabbits awoke from anesthesia. However, the CT scan does not show the materials because both HA and nanoparticles are radiolucent to X-rays. After 12 weeks the control defects remain almost the same, indicating that the bone defect used in this model is critical enough for not being healed after 12 weeks under osteoporotic conditions. The CT scan image for those defects filled with HA also show a radiolucent area at the defect location, evidencing the absence of new bone formation after this period. Only those defects implanted with MBNP and MBNP-IP nanoparticles show X-ray radiopacity after 12 weeks, due to the formation of new bone.

#### 3.3.2. *Histological evaluation and histomorphometric quantification*

Fig. 5 shows the histological images obtained after 12 weeks of implantation. Control and HA samples show hyper-cellular bone marrow. None of these samples show new bone formation or the presence of osteoblast cells lining. The defect site appears colonized by new tissue mainly formed by adipocytes and some inflammatory component in the case of control. On the contrary, animals treated with MBNP and MBNP-IP show new bone formation in the defect location with presence of osteoblasts lining, multinucleated cells identified as osteoclasts and giant cells and histiocytes. The histological images shown in Fig. 6 correspond to representative scenarios for MBNP and MBNP-IP. These images show the newly formed bone (stained in red), which grows around the injected material (stained in pink). The bone tissue shows the characteristic bone structure including osteocytes surrounded by mineralized matrix in both cases, whereas the residual material appears associated to inflammatory component. The expression of CD34 antibodies in the different bone defects are shown in Fig. 7. Control defects (Fig. 7.a) and HA-implanted defects (Fig. 7.b) do not express CD34. In contrast, defects filled with MBNP (Fig. 7.c) and MBNP-IP (Fig. 7.d) show blood vessels stained for CD34.

The expression for CD45 antibodies are shown in Fig. 8. Control defects (Fig. 8.a) show a mild infiltrate of histiocytes among the adipocytes of the bone marrow. The bone defects filled with HA (Fig. 8.b) do not express CD45 antibodies, pointing out the absence of inflammatory response. On the contrary, defects filled with MBNP and MBNP-IP show a moderate infiltration of inflammatory component with a similar staining intensity.

The volume of the defect colonized by new bone after the treatments with the injectable materials is shown in Fig. 9.a. Both MBNP and MBNP-IP promoted bone regeneration after 12 weeks of implantation, colonizing around a 20% of the defect with newly formed bone. The defects implanted only with HA did not show significant differences with the control defects. These results correlate with the trabeculae thickness measurements (Fig. 9.b), as no significant differences were observed between bones treated with MBNP and MBNP-IP injectable materials.

The histological study included the evaluation of the number of osteoblasts (Fig. 9.c) and osteoclasts (Fig. 9.d), as well as the number of blood vessels (Fig. 9.e) and the presence of inflammatory component (Fig. 9.f). The different components were scored semi-quantitatively, according to the parameters listed in Table S1 (see supporting information). The presence of osteoblasts was significantly higher in MBNP-IP compared with MBNP. No osteoblasts were observed in control defects and defects filled with HA. The presence of osteoclasts was marked in the case of defects treated with MBNP and MBNP-IP without showing significant differences between them. Control defects and HA treated defects did not evidence the presence of osteoclasts.

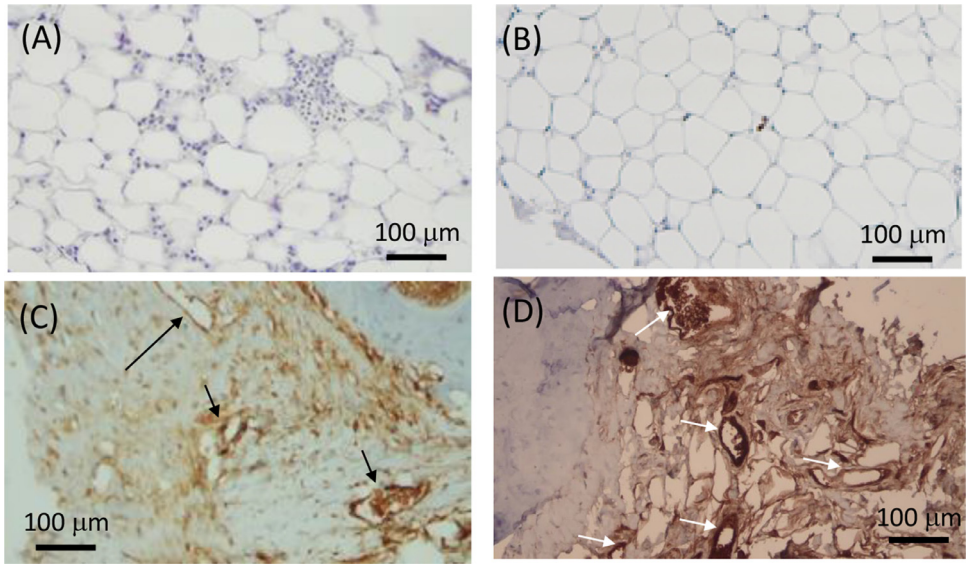


**Fig. 7.** Immunohistochemical staining of bone tissue with CD34 antibodies. (A) Control defect. (B) Hyaluronic acid. (C) Hyaluronic acid with MBNP. (D) Hyaluronic acid with MBNP-IP. Arrows indicate blood vessels.

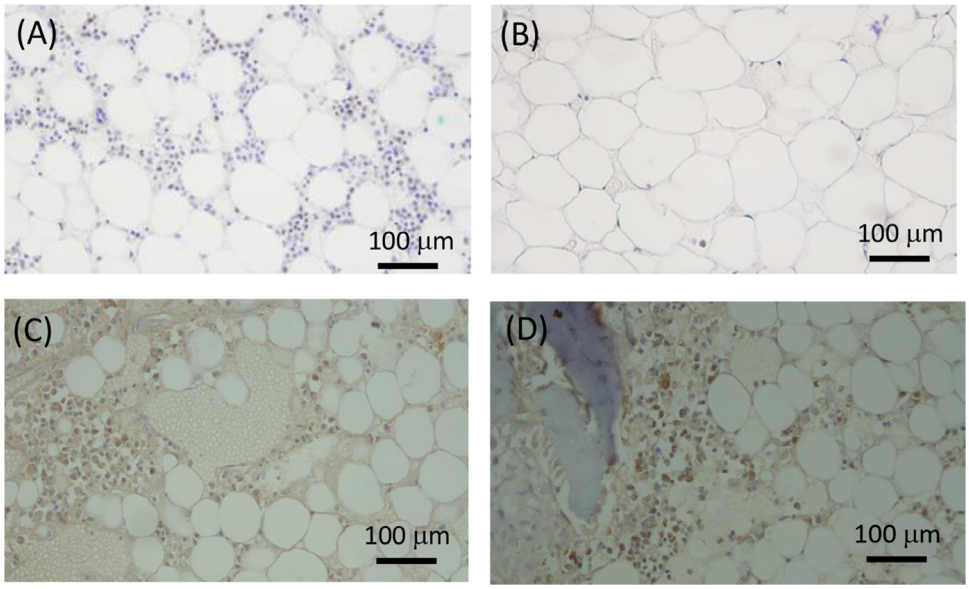


**Fig. 8.** Immunohistochemical staining of bone tissue with CD45 antibodies. (A) Control defect. (B) Hyaluronic acid. (C) Hyaluronic acid with MBNP. (D) Hyaluronic acid with MBNP-IP.

The number of blood vessels in the defects correlated with the values of new bone formation and with the presence of osteoblasts. The control and HA-filled defects did not show angiogenesis, as observed immunohistochemically using CD35 antibody. In contrast, the injectable materials MBNP and MBNP-IP stimulate vascularization, with the MBNP-IP sample scoring significantly higher compared to MBNP. Regarding inflammation, the injectable materials MBNP and MBNP-IP induced a moderate infiltration of inflammatory component. Among the five control defects analyzed, only one of them showed mild histiocyte infiltration, while none of the defects implanted with HA showed the presence of inflammatory component.

## 4. Discussion

The preparation of injectable materials based on bioactive nanoparticles and *in situ* forming hydrogels is a very interesting target in the development of minimally invasive treatments of bone defects and for the primary prevention of fractures in severe osteoporosis scenarios. Among their advantages, injectable bioactive materials can adapt their shape *in situ*, the surgery is much less invasive compared to solid pieces or grafts in the form of granules, and they can be implanted by intraosseous injection in anatomically complex and difficult to access regions. The physical cross-linking that occurs in hydrogels just after implantation facilitates their use as bone fillers and, more specifically, HA has been proposed for the preparation of injectable scaffolds with applications in endodontic [50] and craniofacial regeneration [51]. Bioactive mesoporous nanoparticles are the osteoinductive component of our injectable system. Concentration, size, porosity and morphology are critical factors affecting injectivity. The synthesis strategy based on a dual-template system of PS-b-PAA and CTAB as structure-directing agents results in the formation of spherical mesoporous $SiO_2$–CaO nanoparticles with sizes of 200 nm or less.

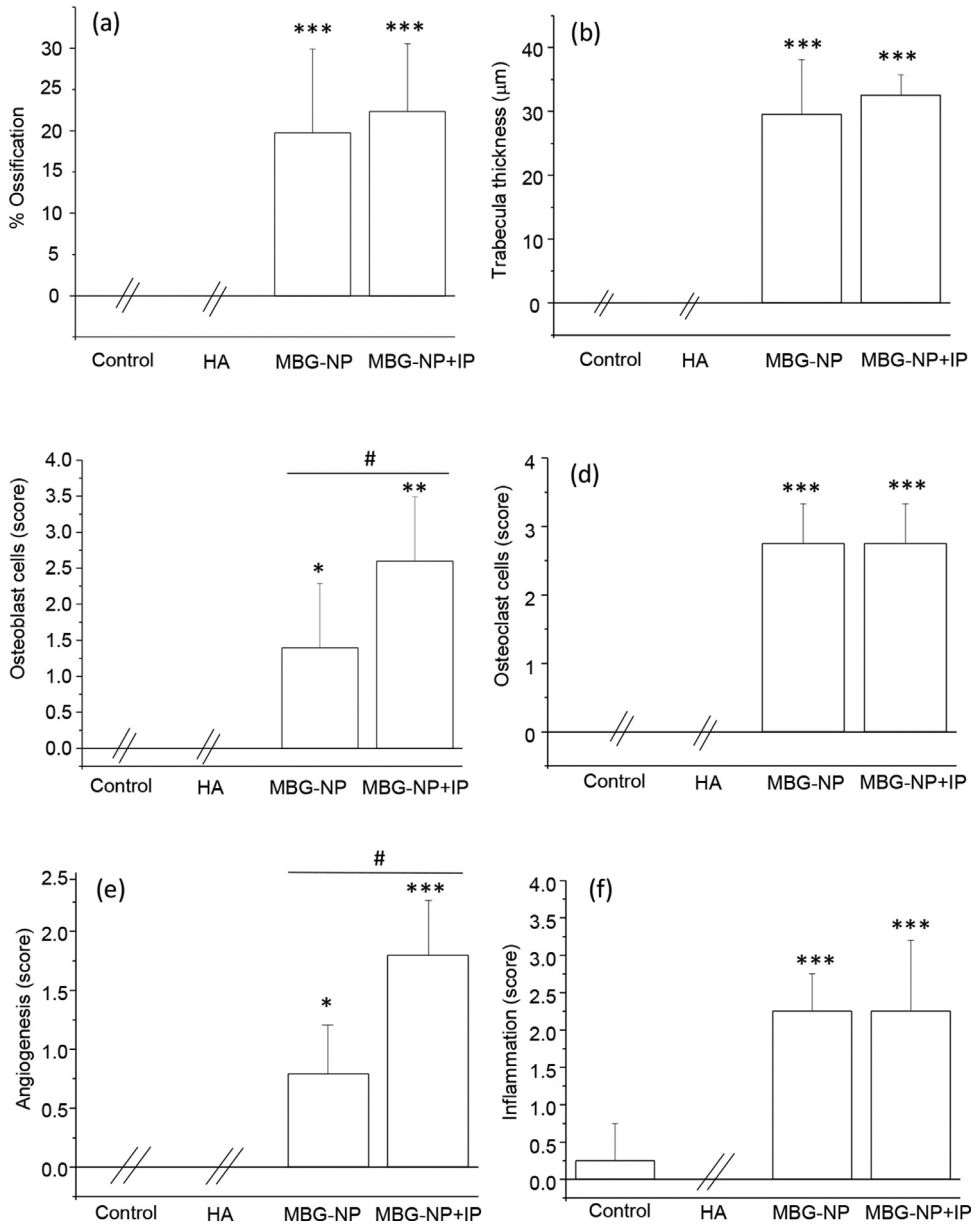


**Fig. 9.** Histomorphometrical studies for the different injectable materials implanted in osteoporotic rabbits. (a) Ossification volume, (b) trabeculae thickness. (c) Osteoblast cells lining (d) Osteoclast cells presence (e) Angiogenesis and (f) Inflammatory component. *Comparison between HA (blank) and nanoparticles containing materials. #Comparison between nanoparticles with and without ipriflavone. Statistical significance: * $p < 0.05$; ** $p < 0.005$: *** $< 0.001$; # $p < 0.05$.

TEM, SEM and $N_2$ adsorption analysis evidence that MSNPs contain two different mesoporous systems. The core of the nanoparticles contains mesopores of 4.3 nm in diameter while the outer shell shows mesopores of 2.6 nm radially distributed around the core. Li *et al.* [29] have proposed a mechanism based on the formation of Ps-b-PAA polymeric aggregates forming the core template, followed by the incorporation of CTAB molecules to form vertical channels in the shell after calcination, as previously observed by López-Noriega *et al.* when they synthesized mesoporous $SiO_2$ microspheres prepared by the aerosol-assisted method [52]. This mesoporous structure allows the incorporation of IP (200 $mg{\cdot}g^{-1}$, normalized by sample amount). IP is a highly non-soluble drug with poor affinity for $SiO_2$ surfaces, which are rich in hydrophilic silanol groups. Despite this low affinity between the drug and the porous matrix, the high surface area and the dual mesoporous system seem to load and retain IP when the drug is dissolved in acetone, exhibiting drug-loading capabilities similar to other mesoporous particles when loaded with more hydrophilic drugs [53].

In the present work, qPCR studies were carried out with the main objective of determining whether the intracellular incorporation of the MSNPs into macrophages could induce the expression of pro-inflammatory genes related not only to pro-inflammatory cytokines (as IL-6 and TNF-$\alpha$) but also to other key molecules involved in signaling pathways for the initiation of an inflammatory response, such as nuclear factor-$\kappa$B1 (NF-$\kappa$B1), the mitogen-activated protein kinase (MAPK) P38 and the inducible nitric-oxide (NO) synthase (iNOS, NOS2). *In vitro* expression of all these pro-inflammatory genes (NF-$\kappa$B1, IL-6, TNF-$\alpha$, P38 and NOS2), points out that these nanoparticles do not show adverse inflammatory effects. These results are in agreement with our previous works, which demonstrated that these nanoparticles did not induce the macrophage polarization towards the M1 pro-inflammatory pheno-

type, favouring the M2 reparative phenotype [41, 54]. On the other hand, MBG nanoparticles were non-inflammagenic for murine lymphoid cells and myeloid dendritic cells [55]. However, MBNPS with or without IP induces a moderate *in vivo* inflammatory response at the injection site, which is absent in the case of bone defects filled with hyaluronic acid alone. Kusaka *et al.* demonstrated that silica particle size influences immune responses [56]. These authors observed that submicron $SiO_2$ particles induce a higher inflammatory response than silica particles with sizes over 1000 nm, showing severe lung inflammation when administered via intra-tracheal. On the other hand, not only the size, but also the shape of nanostructured bioceramics strongly influence the inflammatory response [57]. For instance, 0.1 $\mu$m needle-shaped hydroxyapatite particles induce strong inflammatory response after intraperitoneal injection, which is not observed with spherical particles of comparable size. Our studies indicate that $SiO_2$–CaO mesoporous nanoparticles do not promote the expression of pro-inflammatory genes *in vitro*, and only a moderate presence of histiocytes was observed *in vivo* after 12 weeks of implantation. Certainly, the small size of MBNPs must play an important role in this response, but their spherical shape, the higher biodegradability due to the presence of $Ca^{2+}$ cations and the intraosseous location instead of tracheal or intraperitoneal injection, reduce the severe inflammatory response of MBNPs compared with pure $SiO_2$ or hydroxyapatite nanoparticles. In this context, all particles released by wear of bone-implanted biomaterials are bound to serum proteins forming complexes that are recognized by cell surface receptors or phagocytosed, activating numerous biological pathways in macrophages involved in particle-associated inflammation [58]. The adapter protein Myeloid Differentiation primary response gene 88 (MyD88), and the transcription factor nuclear factor kappa-light-chain-enhancer of activated B cells (NFkB) are key molecules in these events. In our study, the moderate inflammatory response observed *in vivo*, could be due to the interaction of MBNPs with tissue and biological fluid proteins after their bone-implantation. Finally, it is important to highlight that acute inflammation is the first stage in the healing of all tissues, and commonly results in the repair and regeneration of the damaged structures [59].

The HA hydrogel used in this study behaves as an inert material that does not produce osteogenesis or an inflammatory response when injected alone. HA is a natural component found in the extracellular matrix of the human body. It is highly biocompatible and resorbable and has been proposed as a rigid scaffold for bone tissue regeneration [60] and as injectable hydrogels *in situ*, but mostly combined with osteoinductive growth factors or osteogenic cells. Different *in vitro* and *in vivo* studies have demonstrated the ability of HA hydrogels to induce mesenchymal and epithelial cell growth and differentiation, as well as angiogenesis and collagen deposition without producing inflammatory response [61]. In the present study, HA gel injection resulted in partial resorption of the hydrogel and subsequent colonization of the defect by bone marrow adipocytes, without obtaining new bone tissue formation. However, HA hydrogel proved to be a suitable vehicle for injecting bioactive mesoporous nanoparticles, leading to the *in situ* formation of a highly hydrated gel as demonstrated by thermogravimetric analysis of the injectable materials. The *in vivo* experiments carried out in osteoporotic rabbits evidence that MBNPs produce osteogenesis, with the presence of different cell types involved in bone remodeling including osteoblasts, osteoclasts, histiocytes, as well as the formation of blood vessels. Due to the biodegradability and the high water content, HA hydrogel would be highly permeable thus allowing the interaction of MBNPs with the surrounding tissue.

The incorporation of antiosteoporotic drugs in porous implants is a very interesting strategy to carry out the local release of active agents with low bioavailability in bone, as is the case of bisphosphonates, or poorly soluble drugs such as flavonoids. Recently, it has been shown that the incorporation of zoledronic acid, which is a potent inhibitor of bone resorption, in scaffolds made of mesoporous bioactive glasses, inhibited bone tissue regeneration in osteoporotic sheep, despite the potent ostogenic effect of these materials [49]. In this study, the drug incorporated into the nanoparticles was ipriflavone, a highly water-insoluble isoflavone that primarily prevents bone resorption, but also stimulates osteoblast growth and differentiation under *in vitro* conditions. The results of the present study indicate that the presence of PI incorporated into MBNPs results in an increased presence of bone-forming cells in the defect region, as well as increased angiogenesis. This fact coincides with the results obtained *in vitro* with cell cultures that our group performed with preosteoblasts and endothelial progenitor cells (EPCs). The presence of IP in the pores of the MBNPs stimulated the differentiation of MC3T3-E1 osteoprogenitor cells into mature osteoblast phenotype [41] and the expression of VEGFR2 in EPCs [42]. In this sense, a future research line consisting in the incorporation of angiogenic ions such as $Co^{2+}$ and/or $Cu^{2+}$ [62,63] in the chemical composition of our MBNPs could provide better results due to synergistic effects between ipriflavone and these ions. However, the effect on osteogenesis presented by our ipriflavone-loaded nanoparticles is very moderate compared to unloaded particles and cannot be considered significant under the conditions of this study.

## 5. Conclusions

Mesoporous bioactive nanoparticles with core-shell structure and drug loading capability have been synthesized by a double template method.

Mesoporous bioactive nanoparticles do not promote the expression of pro-inflammatory genes under *in vitro* conditions after contact with macrophages.

Mesoporous bioactive nanoparticles promote bone regeneration when injected into osteoporotic bone. The presence of ipriflavone results in a slightly, but not significant, increase of new bone formation and trabeculae thickness. This mild increase of the osteogenic effect could be related with the higher presence of osteoblasts and blood vessels at the implantation site.

The system formed by injectable mesoporous bioactive nanoparticles incorporated in hyaluronic acid is an alternative for minimally invasive surgery treatment of osteoporotic bone.

## Declaration of Competing Interest

The authors declare that they have no known competing financial interests or personal relationships that could have appeared to influence the work reported in this paper.

## Acknowledgements

Animal studies were conducted by the ICTS NANBIOSIS, specifically Units 21, 22, and 24 of the CCMIJU. This research was funded by the projects MAT2016–75611-R, PID2020–11709RB-I00, Advanced Grant VERDI; ERC-2015-AdG Proposal No. 694160. The authors wish to thank the staff of the ICTS Centro Nacional de Microscopía Electrónica (Spain) and the Unidad de Genómica of the Universidad Complutense de Madrid (Spain) for the assistance in the electron microscopy and gene expression studies, respectively.

## Supplementary materials

Supplementary material associated with this article can be found, in the online version, at doi:10.1016/j.actbio.2022.07.067.

## References


[1] P. Mora-Raimundo, D. Lozano, M. Manzano, M. Vallet-Regí, Nanoparticles to Knockdown Osteoporosis-Related Gene and Promote Osteogenic Marker Expression for Osteoporosis Treatment, ACS Nano 13 (2019) 5451–5464.

[2] M. Barry, H. Pierce, L. Cross, M. Tatullo, A.K. Gaharwar, Advances in nanotechnology for the treatment of osteoporosis, Curr. Osteoporos. Rep. 14 (3) (2016) 87–94.

[3] D. Wei, J. Jung, H. Yang, D.A. Stout, L. Yang, Nanotechnology treatment options for osteoporosis and its corresponding consequences, Curr. Osteopor. Rep. 14 (5) (2016) 239–247.

[4] H. Hajiali, L. Ouyang, V. Llopis-Hernández, O. Dobre, F.R.A.J. Rose, Review of emerging nanotechnology in bone regeneration: progress, challenges, and perspectives, Nanoscale 13 (2021) 10266–10280.

[5] D. Arcos, A.R. Boccaccini, M. Bohner, A. Díez-Pérez, M. Epple, E. Gómez-Barrena, A. Herrera, J.A. Planell, L. Rodríguez-Mañas, M. Vallet-Regí, The relevance of biomaterials to the prevention and treatment of osteoporosis, Acta Biomater 5 (10) (2014) 1793–1805.

[6] S.-.S. Li, S.-.H. He, P.-.Y. Xie, W. Li, X.-.X. Zhang, T.-.F. Li, D-F. Li, Recent Progresses in the Treatment of Osteoporosis, Front. Pharmacol. 12 (2021) 717065.

[7] C.H. Kong, C. Steffi, Z. Shi, W. Wang, Development of mesoporous bioactive glass nanoparticles and its use in bone tissue engineering, J. Biomed. Mater Res B. Appl Biomat. 106 (8) (2018) 2878–2887.

[8] Q. Hu, X. Chen, N. Zhao, Y. Li, Facile synthesis and *in vitro* bioactivity of monodispersed mesoporous bioactive glass sub-micron spheres, Mater. Lett 106 (2013) 452–455.

[9] L. Casarrubios, N. Gómez-Cerezo, M.J. Feito, M. Vallet-Regí, D. Arcos, M.Teresa Portolés, Ipriflavone-loaded mesoporous nanospheres with potential applications for periodontal treatment, Nanomaterials 10 (2020) 2573.

[10] J.H. Ahn, I.-.R. Kim, Y. Kim, D-Y. Kim, S.-.B. Park, B.-.S. Park, M.-.K. Bae, Y.-.I. Kim, Yong-Il. The effect of mesoporous bioactive glass nanoparticles/graphene oxide composites on the differentiation and mineralization of human dental pulp stem cells, Nanomaterials 10 (4) (2020) 620.

[11] S.Y. Park, K.-.H. Yoo, S.-.Y. Yoon, W.-.S. Son, Y.-.I. Kim, Synergetic effect of 2-methacryloyloxyethyl phosphorylcholine and mesoporous bioactive glass nanoparticles on antibacterial and anti-demineralisation properties in orthodontic bonding agents, Nanomaterials 10 (7) (2020) 1282.

[12] H. Sun, K. Zheng, T. Zhou, A.R. Boccaccini, Incorporation of zinc into binary $SiO_2$-CaO mesoporous bioactive glass nanoparticles enhances anti-inflammatory and osteogenic activities, Pharmaceutics 13 (12) (2021) 2124.

[13] F. Westhauser, F. Rehder, S. Decker, E. Kunisch, A. Moghaddam, K. Zheng, A.R. Boccaccini, Ionic dissolution products of Cerium-doped bioactive glass nanoparticles promote cellular osteogenic differentiation and extracellular matrix formation of human bone marrow derived mesenchymal stromal cells, Biomed Mater 16 (3) (2021) 035028.

[14] F. Westhauser, S. Decker, Q. Nawaz, F. Rehder, S. Wilkesmann, A. Moghaddam, E. Kunisch, A.R. Boccaccini, Impact of zinc- or copper-doped mesoporous bioactive glass nanoparticles on the osteogenic differentiation and matrix formation of mesenchymal stromal cells, Materials (Basel) 14 (8) (2021) 1864.

[15] M. Ravanbakhsh, S. Labbaf, F. Karimzadeh, A. Pinna, A.B. Houreh, M.H. Nasr-Esfahani, Mesoporous bioactive glasses for the combined application of osteosarcoma treatment and bone regeneration, Mater Sci Eng C Mater Biol Appl 104 (2019) 109994.

[16] M. Hu, J. Fang, Y. Zhang, X. Wang, W. Zhong, Z. Zhou, Design and evaluation a kind of functional biomaterial for bone tissue engineering: selenium/mesoporous bioactive glass nanospheres, J. Colloid Interf. Sci. 579 (2020) 654–666.

[17] D. Marovic, H.J. Haugen, V.N. Mandic, M. Par, K. Zheng, Z. Tarle, A.R. Boccaccini, Incorporation of copper-doped mesoporous bioactive glass nanospheres in experimental dental composites: chemical and mechanical characterization, Materials (Basel) 14 (10) (2021) 2611.

[18] F. Kurtuldu, H. Kankova, A.M. Beltran, L. Liverani, D. Galusek, A.R. Boccaccini, Anti-inflammatory and antibacterial activities of cerium-containing mesoporous bioactive glass nanoparticles for drug-free biomedical applications, Materials Today Bio 12 (2021) 100150.

[19] K. Zheng, P. Balasubramanian, T.E. Paterson, R. Stein, S. MacNei, S. Fiorilli, C. Vitale-Brovarone, J. Shepherd, A.R. Boccaccini, Ag modified mesoporous bioactive glass nanoparticles for enhanced antibacterial activity in 3D infected skin model, Mater Sci Eng C Mater Biol Appl 103 (2019) 109764.

[20] A. Bari, N. Bloise, S. Fiorilli, G. Novajra, M. Vallet-Regi, G. Bruni, A. Torres-Pardo, J.M. Gonzalez-Calbet, L. Visai, C. Vitale-Brovarone, Copper-containing mesoporous bioactive glass nanoparticles as multifunctional agent for bone regeneration, Acta Biomater 55 (2017) 493–504.

[21] Y. Zhang, M. Hu, W. Zhang, X. Zhang, Construction of tellurium-doped mesoporous bioactive glass nanoparticles for bone cancer therapy by promoting ROS-mediated apoptosis and antibacterial activity, J Colloid Interf Sci 610 (2022) 719–730.

[22] Y. Zhang, M. Hu, W. Zhang, X. Zhang, Xiaona, Homology of selenium (Se) and tellurium (Te) endow the functional similarity of Se-doped and Te-doped mesoporous bioactive glass nanoparticles in bone tissue engineering, Ceram Int 48 (2022) 3729–3739.

[23] A. El-Fiqi, R. Allam, H.-.W. Kim, Antioxidant cerium ions-containing mesoporous bioactive glass ultrasmall nanoparticles: structural, physico-chemical, catalase-mimic and biological properties, Colloid Surf B. Biointerf 206 (2021) 111932.

[24] A. El-Fiqi, H.-.W. Kim, Sol-gel synthesis and characterization of novel cobalt ions-containing mesoporous bioactive glass nanospheres as hypoxia and ferroptosis-inducing nanotherapeutics, J Non-Cryst Solids 569 (2021) 120999.

[25] L.M. Mukundan, S. Dhara, S. Chattopadhyay, Trimodal attributes within acidic mesostructured bioactive glass nanoparticles, Mater. Letters 293 (2021) 129667.

[26] Z. Nescakova, K. Zheng, L. Liverani, Q. Nawaz, D. Galuskova, H. Kankova, M. Michalek, D. Galusek, A.R. Boccaccini, Multifunctional zinc ion doped sol - gel derived mesoporous bioactive glass nanoparticles for biomedical applications, Bioactive Mater 4 (2019) 312–321.

[27] Q. Liang, Q. Hu, G. Miao, B. Yuan, X. Chen, A facile synthesis of novel mesoporous bioactive glass nanoparticles with various morphologies and tunable mesostructured by sacrificial liquid template method, Mater. Letters 148 (2015) 45–49.

[28] D. Arcos, A. López-Noriega, E. Ruiz-Hernández, O. Terasaki, M. Vallet-Regí, Ordered mesoporous microspheres for bone grafting and drug delivery, Chem. Mater. 21 (6) (2009) 1000–1009.

[29] Y. Li, B.P. Bastakoti, Y. Yamauchi, Smart soft-templating synthesis of hollow mesoporous bioactive glass spheres, Chem. Eur. J. 21 (2015) 8038–8042.

[30] X. Ding, J. Zheng, F. Ju, L. Wang, J. Kong, J. Feng, T. Liu, Facile fabrication of hollow mesoporous bioactive glass spheres: from structural behaviour to *in vitro* biology evaluation, Ceram Int 47 (24) (2021) 34836–34844.

[31] N. Mutlu, A.M. Beltran, Q. Nawaz, M. Michalek, A.R. Boccaccini, K. Zheng, Combination of selective etching and impregnation toward hollow mesoporous bioactive glass nanoparticles, Nanomaterials 11 (7) (2021) 1846.

[32] Y. Wang, H. Pan, X. Chen, The preparation of hollow mesoporous bioglass nanoparticles with excellent drug delivery capacity for bone tissue regeneration, Front. Chem. 7 (2019) 283.

[33] X. Li, G. Miao, X. Chen, G. Yuan, H. Liu, C. Mao, X. Shen, C. Ning, Investigation of radial mesoporous bioactive glass particles as drug carriers for inhibition of tumor cells, Sci. Adv. Mater. 9 (2017) 562–570.

[34] X. Li, X. Chen, G. Miao, H. Liu, C. Mao, G. Yuan, Q. Liang, X. Shen, C. Ning, X. Fu, Synthesis of radial mesoporous bioactive glass particles to deliver osteoactivin gene, J. Mater. Chem. B 2 (2014) 7045–7054.

[35] C. Pontremoli, M. Boffito, S. Fiorilli, R. Laurano, A. Torchio, A. Bari, C. Tonda–Turo, G. Ciardelli, C. Vitale-Brovarone, Hybrid injectable platforms for the *in situ* delivery of therapeutic ions from mesoporous glasses, Chem. Eng. J. 340 (2018) 103–113.

[36] A. El-Fiqi, N. Mandakhbayar, S.B. Jo, J.C. Knowles, J.H. Lee, H.W. Kim, Nanotherapeutics for regeneration of degenerated tissue infected by bacteria through the multiple delivery of bioactive ions and growth factor with antibacterial/angiogenic and osteogenic/odontogenic capacity, Bioactive Mater 6 (1) (2021) 123–136.

[37] B. Sui, X. Liu, J. Sun, Dual-functional dendritic mesoporous bioactive glass nanospheres for calcium influx-mediated specific tumor suppression and controlled drug delivery *in vivo*, ACS Appl. Mater. Interf. 10 (28) (2018) 23548–23559.

[38] M.S. Kang, N.-.H. Lee, R.K. Singh, N. Mandakhbayar, R.A. Perez, J.-.H. Lee, H.-.W. Kim, Nanocements produced from mesoporous bioactive glass nanoparticles, Biomaterials 162 (2018) 183–199.

[39] J.-.H. Lee, N. Mandakhbayar, A. El-Fiqi, H.-.W. Kim, Intracellular co-delivery of Sr ion and phenamil drug through mesoporous bioglass nanocarriers synergizes BMP signaling and tissue mineralization, Acta Biomater 60 (2017) 93–108.

[40] B. Sui, G. Zhong, J. Sun, Drug-loadable mesoporous bioactive glass nanospheres: biodistribution, clearance, BRL cellular location and systemic risk assessment via Ca-45 labelling and histological analysis, Sci. Rep. 6 (2016) 33443.

[41] L. Casarrubios, N. Gómez-Cerezo, M.J. Feito, M. Vallet-Regí, D. Arcos, M.T. Portolés, Incorporation and effects of mesoporous $SiO_2$-CaO nanospheres loaded with ipriflavone on osteoblast/osteoclast cocultures, Eur. J. Pharm. Biopharm. 133 (2018) 258–268.

[42] L. Casarrubios, A. Polo-Montalvo, M.C. Serrano, M.J. Feito, M. Vallet-Regí, D. Arcos, M.T. Portolés, Effects of ipriflavone-loaded mesoporous nanospheres on the differentiation of endothelial progenitor cells and their modulation by macrophages, Nanomaterials 11 (2021) 1102.

[43] R. Civitelli, In Vitro and *in vivo* effects of ipriflavone on bone formation and bone biomechanics, Calcif. Tissue. Int. 61 (1997) S12—S14.

[44] J-Y.L. Reginster, Ipriflavone: pharmacological properties and usefulness in postmenopausal osteoporosis, Bone Miner 23 (1993) 223–232.

[45] S.H. Kima, M.G. Leeb, Pharmacokinetics of ipriflavone, an isoflavone derivative, after intravenous and oral administration to rats hepatic and intestinal first–pass effects, Life Sci 70 (2002) 1299–1315.

[46] J. Kim, I.S. Kim, T.H. Chod, K.B. Lee, S.J. Hwang, G. Tae, I. Noh, S.H. Lee, Y. Park, K. Sun, Bone regeneration using hyaluronic acid-based hydrogel with bone morphogenic protein-2 and human mesenchymal stem cells, Biomaterials 28 (2007) 1830–1837.

[47] P. Zhai, X. Peng, B. Li, Y. Liu, H. Sun, Xi. Li, The application of hyaluronic acid in bone regeneration, Int. J Biol. Macromol. 151 (2020) 1224–1239.

[48] S. Castañeda, E. Calvo, R. Largo, R. González-González, C. de la Piedra, M. Díaz-Curiel, G. Herrero-Beaumont, Characterization of a new experimental model of osteoporosis in rabbits, J Bone Miner Metab 26 (1) (2008) 53–59.

[49] N. Gómez-Cerezo, L. Casarrubios, M. Saiz-Pardo, L. Ortega, D. de Pablo, I. Díaz-Güemes, B. Fernández-Tomé, S. Enciso, F.M. Sánchez-Margallo, M.T. Portolés, D. Arcos, M. Vallet-Regí, Mesoporous bioactive glass/ε-polycaprolactone

scaffolds promote bone regeneration in osteoporotic sheep, Acta Biomater 90 (2019) 393–402.
[50] C.R. Silva, P.S. Babo, M. Gulino, L. Costa, J.M. Oliveira, J. Silva-Correia, R.M.A. Domingues, R.L.-. Reis, M.E. Gomes, Injectble and tunable hyaluronic acid hydrogels releasing chemotactic and angiogenic growth factores for endodontic regeneration, Acta Biomater 77 (2018) 155–171.
[51] B. Chang, H. Ahuja, C. Ma, X. Liu, Injectable scaffolds: preparation and application in dental and craniofacial regeneration, Mater. Sci. Eng. R Rep. 111 (2017) 1–26.
[52] A. López-Noriega, E. Ruiz-Hernández, S.M. Stevens, D. Arcos, M.W. Anderson, O. Terasaki, M. Vallet-Regí, Mesoporous Microspheres with Doubly Ordered Core– Shell Structure, Chem. Mater 21 (2009) 18–20.
[53] M. Vallet-Regí, F. Balas, D. Arcos, Mesoporous Materials for drug delivery, Angew. Chem. Int. Ed. 46 (2007) 7548–7558.
[54] M.J. Feito, L. Casarrubios, M. Oñaderra, M. Gómez-Duro, P. Arribas, A. Polo–Montalvo, M. Vallet-Regí, D. Arcos, M.T. Portolés, Response of RAW 264.7 and J774A.1 macrophages to particles and nanoparticles of a mesoporous bioactive glass: a comparative study, Colloid Surf B. Biointerf. 208 (2021) 112110.
[55] M. Montes-Casado, A. Sanvicente, L. Casarrubios, M.J. Feito, J.M. Rojo, M. Vallet-Regí, D. Arcos, P. Portolés, M.T. Portolés, An immunological approach to the biocompatibility of mesoporous $SiO_2$-CaO nanospheres, Int. J. Mol. Sci. 21 (2020) 8291.
[56] T. Kusaka, M. Nakayama, K. Nakamura, M. Ishimiya, E. Furusawa, K. Ogasawara, Effect of Silica Particle Size on Macrophage Inflammatory Responses, PLoS ONE 9 (2014) e92634.
[57] F. Lebre, R. Sridharan, M.J. Sawkins, D.J. Kelly, F.J. O'Brien, Ed C. Lavelle, The shape and size of hydroxyapatite particles dictate inflammatory responses following implantation, Sci. Rep. 7 (2017) 2922.
[58] S.B. Goodman, J. Pajarinen, Z. Yao, T. Lin, Inflammation and Bone Repair: from Particle Disease to Tissue Regeneration, Front. Bioeng. Biotechnol. 7 (2019) 230.
[59] A. Mantovani, S.K. Biswas, M.R. Galdiero, A. Sica, M. Locati, Macrophage plasticity and polarization in tissue repair and remodelling, J. Pathol. 229 (2013) 176–185.
[60] P.T. Sudheesh Kumar, S. Hashimi, S. Saifzadeh, S. Ivanovski, C. Vaquette, Additively manufactured biphasic construct to loaded with BMP-2 for vertical bone regeneration: a pilot study in rabbit, Mater. Sci. Eng. C 92 (2018) 554–564.
[61] L. Zhang, U. D'Amora, A. Ronca, Y. Li, X. Mo, F. Zhou, M. Yuan, L. Ambrosio, J. Wu, M.G. Raucci, *In vitro* and *in vivo* biocompatibility and inflammation response of methacrylated and maleated hyaluronic acid for wound healing, RSC Adv 10 (2020) 32183.
[62] C. Wu, Y. Zhou, M. Xu, P. Han, L. Chen, J. Chang, Y. Xiao, Copper-containing mesoporous bioactive glass scaffolds with multifunctional properties of angiogenesis capacity, osteostimulation and antibacterial activity, Biomaterials 34 (2013) 422–433.
[63] C. Wu, Y. Zhou, W. Fan, P. Han, J. Chang, J. Yuen, M. Zhang, Y. Xiao, Hypoxia-mimicking mesoporous bioactive glass scaffolds with controllable cobalt ion release for bone tissue engineering, Biomaterials 33 (2012) 2076–2085.